7

SEMPA Studies of Thin Films, Structures, and Exchange Coupled Layers

H.P. Oepen and H. Hopster

Scanning electron microscopy with polarization analysis (SEMPA) has developed into a powerful technique to study domains in ultrathin films. In this chapter, we discuss from a very general point of view the instrumental aspects of the method. Examples of thin film investigations are given that demonstrate unique features of SEMPA. New solutions around apparent limitations of the technique are presented at the end, i.e., analyzing samples with contaminated surfaces and imaging in external fields.

7.1 Introduction

In 1982, triggered by the investigations of the energy dependence of the spin-polarization of secondary electrons (SE), the idea emerged to use this effect in a microscope to image magnetic structures [1,2]. The combination of a conventional **S**canning **E**lectron **M**icroscope (SEM) and a spin-polarization analyzer promised the potential of investigating magnetic microstructures with high spatial resolution. In 1984, the first **spin-SEM** was realized by Koike and coworkers [3], followed less than one year later by a microscope built at NIST [4]. The latter group introduced the abbreviation **SEMPA**, which stands for **S**canning **E**lectron **M**icroscope with **P**olarization **A**nalysis. We will use both acronyms interchangeably. The next instruments followed in Europe [5,6]. A sketch of SEMPA is given in Fig. 7.1. Due to the low depth of information, ultra-clean surfaces are essential, requiring ultrahigh vacuum (UHV) conditions. Since conventional SEMs usually do not operate in UHV, appropriate UHV-compatible columns (or guns) are rare and expensive. Hooked on is the detector system that consists of an electron optic and a spin-polarization analyzer. The optic has to focus the secondaries into the polarization analyzer. The most important feature of the electron optic is the acceptance angle for SE. It is extremely important that the optic collects electrons emitted in the full 2π solid angle.

Several microscopes have been realized [7–14], and a few more have been proposed. Basically, all the systems look very similar. Some have attachments for surface

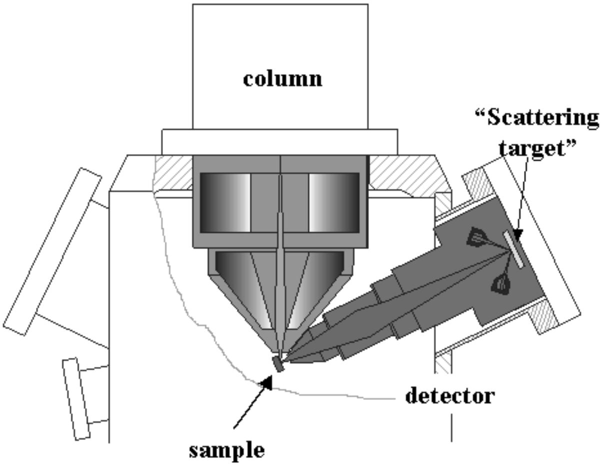

Fig. 7.1. Sketch of SEMPA. The electron microscope column gives a narrow primary electron beam that creates secondary electrons at the sample. The secondary electrons are focused onto a scattering target, and scattered intensities are measured. The scattering targets and energies differ in the various SEMPA depending on the polarization analyzer used. The whole system works under ultrahigh vacuum conditions

preparation or to grow films in situ. Most of the microscopes use a Mott spin-polarization analyzer based on the scattering of electrons off a gold film at energies from $20-100\,\mathrm{KeV}$ [15–17]. Two groups use different kinds of low energy spin-polarization analyzers. In the NIST system, the low energy diffuse scattering from Au is used to perform spin analysis [18,19]. The microscopes at MPI in Halle [14] and Hamburg [5] are equipped with the LEED spin-polarization analyzer (**L**ow **E**nergy **E**lectron **D**iffraction) [20,21].

In the beginning, semi-infinite samples were studied, focusing on devices [22,23], or surface properties of bulk systems like the microstructure of domain walls [24–26]. The unique properties of the technique have been discussed by the various groups [5, 6,22,23,27]. The biggest advantage of SEMPA is that the orientation of magnetization can be measured directly via the spin-polarization of the secondaries, since the spin-polarization vector is anti-parallel to the magnetization [28]. The polarization orientation is achievable since most of the analyzers measure two perpendicular polarization components simultaneously. It is a question of geometry then to obtain full vector information. In a more sophisticated setup, one can use two perpendicular spin analyzers yielding access to all three components, though not truly simultaneously since one has to switch between the two detectors. In two SEMPA systems, this has been realized [5,29], while another approach is to use a spin-rotator [30] within the optics [13, 30]. Another advantage of the spin-SEM is the high surface sensitivity that allows imaging of domain structure in ultrathin films, i.e., films with thicknesses of a few monolayers [31–33]. The spatial resolution has been improved to 20 nm by establishing second-generation microscopes [34]. Recently, a resolution of about

5 nm has been reported for the third generation of spin-SEM [35]. This is competitive with the resolution of Lorentz microscopy (see Chap. 4 in this book).

Some of the setups have been described in detail, discussing the specifications of every component of the microscope [5,23,29,36]. In the following, we would like to concentrate on the essential features that can be deduced from general considerations about the physical processes involved. We will stick to the situation of the microscope operating in the counting mode, as in most of the existing SEMPAs the signal is very low. The reasons for this are the low intensity of SEM primary beams and the extremely low efficiency of spin-analyzers. The statistical error in the measurement of polarization [15] δP is

$$\delta P = 1/\sqrt{F\,J\,t}\,, \tag{7.1}$$

with F the figure of merit and J the electrons per second entering the detector and t the measuring time per pixel. The figure of merit describes the overall efficiency of a detector. It is

$$F = S^2\,\eta\,, \tag{7.2}$$

with S being the Sherman function, which describes the polarization sensitivity, i.e., how well the detector separates spin-up and spin-down electrons, and η the reflectivity, i.e., the number of electrons detected divided by the total number of electrons entering the detector [5,22,23]. From this, the relative error in polarization detection $\delta P/P$ is

$$\frac{\delta P}{P} = \frac{1}{P\sqrt{F\,J\,t}}\,, \tag{7.3}$$

which determines the relative precision. This quantity sets the ultimate limit of what can be resolved as the smallest change in polarization and thus in magnetic structure. The inverse quantity is more common in SEM, i.e., the contrast that can be achieved [5,22,23]. The formula is important for spin-SEM, and it is the fundamental expression for the following discussion. The performance of the entire system is determined by its three components: gun as the excitation source, secondary electron emission processes, and the spin detection system. We will discuss these in the next sections.

7.2 Instrumentation

7.2.1 Basics: Secondary Electron Emission

We will use the intensity distribution and the spin polarization of the secondaries to work out some general features for a SEMPA system (always concentrating on the case of Fe). The intensity distribution of the secondary electrons is well known from scanning electron microscopy [37]. The energy dependence is described by an analytic function:

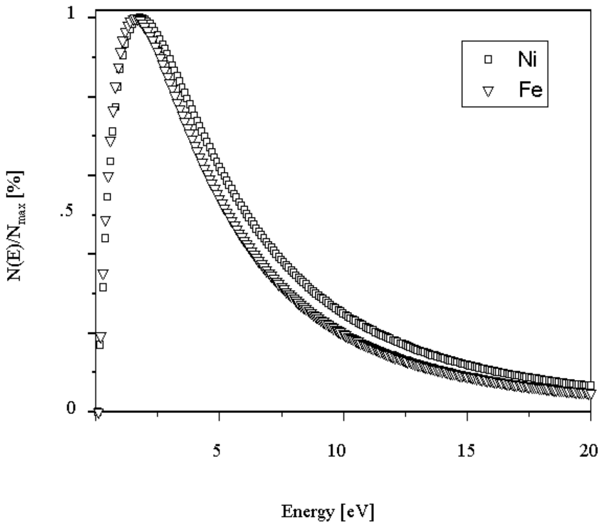

Fig. 7.2. Intensity distribution of secondary electrons. The graph is normalized to the value of the maximum of the distribution. The work function for Fe (Ni) are 4.5 eV (5.15 eV), taken from [123]

$$N(E) \propto E/(E+\Phi)^4 \,, \tag{7.4}$$

with E the energy of the secondaries and Φ the work function of the material. $N(E)$ is plotted for Ni and Fe in Fig. 7.2. Energy resolved spin polarizations have been measured for Fe, Co, Ni, and also alloys [38–40]. In all cases there is a strong spin polarization enhancement at very low energies. In Ni [40] this feature is very sharp, while in Fe it is much broader [41]. As $P(E)$ depends on the excitation energy [42], we chose measurements for excitation energies well above 1000 eV. Figure 7.3 shows a fit according to

$$P_n(E) = P_1 + P_2 \exp(-E/E_H) \,, \tag{7.5}$$

with the parameters $P_{1,2}$ and E_H given in the figure caption.

It is most fortunate that high intensity and high polarization are both found at very low SE energies. Thus, it is clear that a SEMPA system has to analyze the very low energy secondaries. On the other hand, the energy distribution is quite broad, which can pose experimental problems with electron optics. The question arises: What are the optimum performance conditions. The relevant quantity for counting statistics is P^2J.

With the model curves for $P(E)$ and $J(E)$ (i.e., $N(E)$ from Fig. 7.2), we can calculate what can be achieved. We model the energy acceptance by a window over energy interval of width D centered about a mean pass energy E_D. For the sake of simplicity we assume normal emission and full acceptance of the electrons emitted into $\Omega = 2\pi$ and a transmission of 100% within the energy window and zero outside.

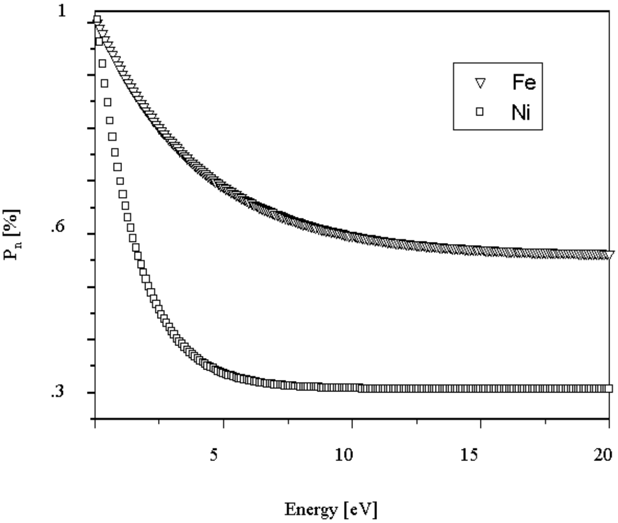

Fig. 7.3. Normalized secondary electron polarization. The *curves* are obtained by fitting experimental *curves* from [40,41]. For $P_n = P/P_0$ ($P_0 =$ is the polarization at zero energy) and the energy dependence $P_\mathrm{n}(E) = P_1 + P_2\ \exp(-E/E_H)$, we obtain for Fe (Ni) the following fitting parameters. $P_1 = 0.56$ (0.3075), $P_2 = 0.44$ (0.6984), and $E_\mathrm{H} = 4\,\mathrm{eV}$ (1.56 eV)

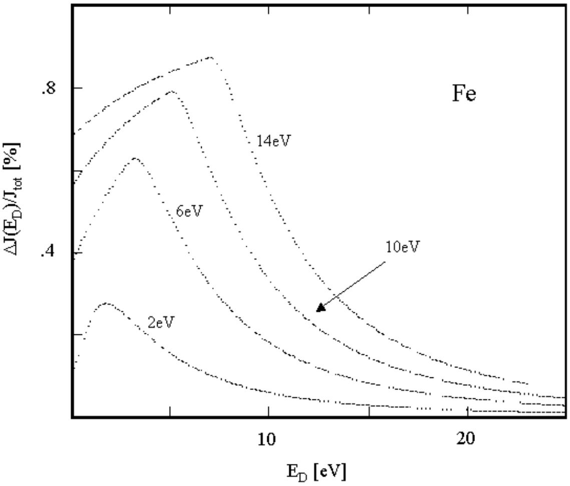

Fig. 7.4. Secondary electron intensity ΔJ for given energy window D versus pass energy E_D. The different energy intervals D are given as parameters in the plot. The intensity is normalized to the total secondary electron intensity, i.e., the intensity between $0-50\,\mathrm{eV}$

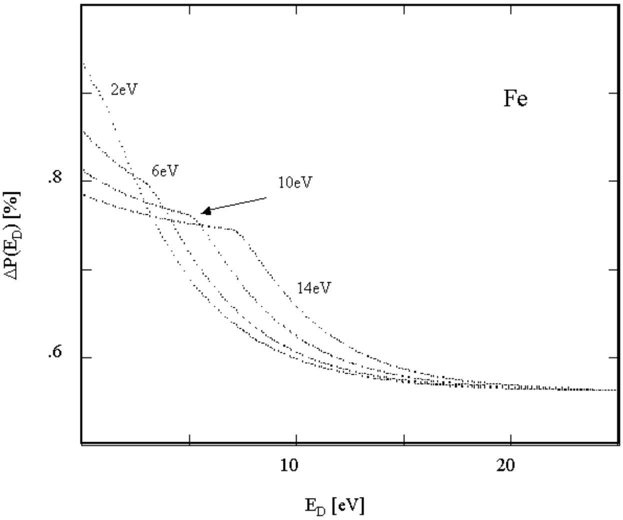

Fig. 7.5. Secondary electron polarization ΔP for given energy window D versus pass energy E_D. The different D are given as parameters in the plots. The graphs have been attained utilizing the P_n distributions from Fig. 7.3

The results of this averaging is shown in Fig. 7.4 and Fig. 7.5 for the intensity and polarization, respectively. With these results, $\Delta P^2 \Delta J$ can be calculated, which is shown in Fig. 7.6 as a function of pass energy, with the energy width as a parameter. Figures 7.4 and 7.6 show very similar overall shape. From the experimental point of view this is an extremely important feature. It means for any SEMPA tuning with given energy spread the system should be assembled in such a way as to find the intensity maximum, which is automatically the maximum of the quantity $P^2 J$. It is not necessary to measure polarization in finding optimal performance. This fact makes a real-time tuning feasible.

From the above considerations about the transmitted intensity and polarization one can derive important conclusions for designing a new microscope and its operation characteristics:

1. Figure 7.6 directly indicates that it is not desirable to select an energy spread that is very small, as this costs a lot of performance. The microscope becomes very delicate to handle, as $\Delta P(E)$ is extremely sensitive to any change of E_D. This will contribute to apparatus asymmetries. A sophisticated energy spectrometer is necessary to prevent such problems [7, 10].
2. On the other hand, it is also not necessary to take ΔE_D too large. The gain in the relevant quantity $\Delta P^2 \Delta J$ is very low above $\Delta E_D = 10\,\mathrm{eV}$. From Fig. 7.6 the increase is about 5% going from $\Delta E_D = 10\,\mathrm{eV}$ to $\Delta E_D = 14\,\mathrm{eV}$, while it is 12.7% for changing from 6 to 10 eV. A problem of the large energy spread is that it becomes difficult to attain the full emission angle for higher electron

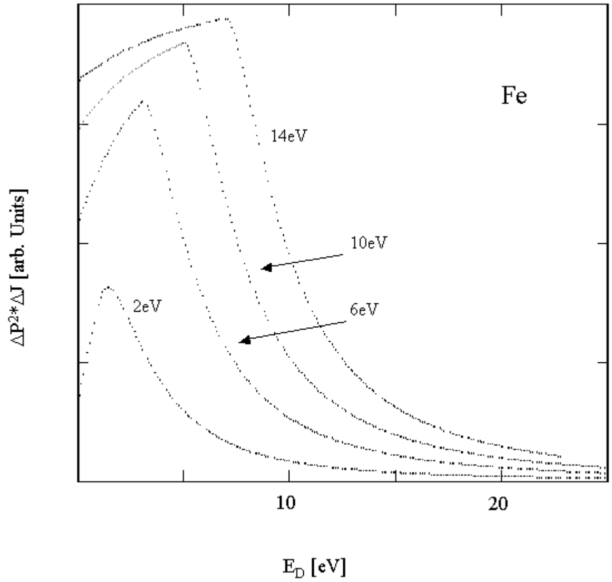

Fig. 7.6. The product of ΔP^2 and ΔJ versus E_D for Fe. D is given as a parameter in the plot.

energies. This effect will reduce the nominal gain, which is given in the above calculations for the ideal system. The optical problems of focusing the electrons into the spin-analyzer will also rise considerably due to chromatic aberration of the electron optics.

3. These considerations reveal that it is favorable to select an energy spread of $\Delta E_D = 6-10$ eV, which has to be handled by the attached detector system. Some of the SEMPA systems have been characterized by energy spreads that lie within this span [5, 29].

7.2.2 Spin-Polarization Analyzer

A major point in SEMPA design is the energy width of the detector system. What is the energy spread the spin-polarization analyzer can tolerate for desired specifications, i.e., figure of merit F and/or sensitivity S. Or, vice versa, what degradation of performance of the polarization analyzer does the desired energy width cause. The latter consideration immediately excludes spin-polarization analyzers that need very sharp energy distributions, like analyzers utilizing scattering at very low energies [43–46]. The compromise that has to be made with such analyzers will be considerably worse than utilizing detectors that accept a very broad energy distribution without loss of performance, like the Mott-polarimeter [13, 15] or the Low Energy Diffuse Scattering spin analyzer (LEDS) [19, 22]. With such analyzers, however, the energy width is defined by another element of the detector system. This can be the focusing optics, due to its chromatic aberration or an energy analyzer that is incorporated into the system prior to the polarization analysis [5, 7, 10]. In the latter case, a stable situation is achieved. In the former case, however, the detector system will show more or less strong dependence on the imaging condition of the optics and most often on the lateral position of the point of electron emission (due to the scanning of the primary beam) [29]. The handling of the spin-SEM can become very delicate, as any change of the electron trajectories can change ΔE_D, which causes ΔP to vary. A position-dependent apparatus asymmetry is the consequence. Particularly, when the detector sensitivity is not high, this can cause severe problems. Very sophisticated beam corrections (steering) are necessary to minimize such unwanted effects. An excellent solution to this problem with a perfect correction has been incorporated into the NIST microscope [29]. An alternative is to use a polarization analyzer that works as its own energy filter with desired energy spread. This can be achieved, for example, by an appropriate geometrical layout of the LEED-detector [20, 47] utilizing the low energy diffraction of electrons to perform as the energy dispersive element. If an active energy analyzer is incorporated, the optics should provide 100% transmission at least over the same energy window.

Now we can put the results of the two previous sections together and discuss the consequences with respect to the spin analyzers and electron sources. With the values ΔP and ΔJ averaged over the energy window, the relative error of polarization detection is

$$\frac{\delta P}{P} = \frac{1}{\Delta P \sqrt{F\,\Delta J\,t}} \,. \tag{7.6}$$

Common to all spin-polarization analyzers is a very low efficiency of about $F = 10^{-4}$, which is surprisingly similar for all kinds of analyzers used in spin-SEM [5,16,17,29,34,36]. Many attempts have been made to overcome this problem. Some analyzers with slightly higher efficiency have been reported [43–46]. Besides the problems due to the small energy spread allowed, the other issue in SEMPA is polarization vector analysis. While the analyzers currently used in SEMPA give access to two polarization components simultaneously, the new analyzer designs are sensitive to only one component at a time. Putting $F = 10^{-4}$ into the formula we obtain

$$\frac{\delta P}{P} = \frac{100}{\Delta P \sqrt{\Delta J\,t}} \,. \tag{7.7}$$

Next, we will make a best-case approximation in the sense that we assume the highest ΔP that can be observed. This is found for clean Fe surfaces. For the ideal detector tuned to the optimum ΔE_D range one can expect for Fe with the polarization of $P_0 = 50\%$ at zero energy (see Fig. 7.5) [1]

---

[1] For Ni it is worse. Due to the strong reduction of the polarization when averaging over the energy window and the low value of P_0, the polarization becomes $\Delta P = 0.085$. For comparison, the ratio of the polarization values

$$\frac{\Delta P_{\mathrm{Ni}}}{\Delta P_{\mathrm{Fe}}} = \frac{1}{4.7}$$

is most important.

$$\Delta P = 0.8 \times P_0 = 0.4 \tag{7.8}$$

and thus

$$\frac{\delta P}{P} = \frac{250}{\sqrt{\Delta J\, t}} \,. \tag{7.9}$$

If we want to have a relative accuracy of 10% (which means in SEM terms a contrast of 10) we end up with

$$\Delta J\, t = 6.25 \times 10^6 \tag{7.10}$$

When imaging magnetic microstructures it is highly desirable to keep the dwell time as short as possible. Favorable dwell times are in the range of milliseconds, which immediately puts ΔJ, the electrons per second entering the detector, into the range of 10^{10} counts/s. As the reflectivity η is in the range of 10^{-3} for most of the analyzers, it puts the limits on the counting facilities. Obviously, in high-end systems counting must be fast and the equipment should at least handle count rates up to 10 MHz without problems. Limits are pushed even higher, and problems can arise if η is higher, which is true for the LEDS-detector [18, 19]. Switching to an analog operation mode can become necessary [29]. A low reflectivity means that the polarization sensitivity is higher and vice versa for analyzers with similar efficiency ($F = 10^{-4}$). A higher sensitivity, S, minimizes problems with apparatus asymmetry, the lower reflectivity fits better the working range for pulse counting when using the best columns available at the moment. Hence, it is advisable to select the analyzer that has the higher spin sensitivity (S) and the lower reflectivity to prevent severe difficulties.

7.2.3 Electron Column

SE-detectors used in conventional SEM typically have an efficiency close to 100%. A high probe current is usually not a design criterion of highest priority for SE-columns. Consequently, only very few columns are commercially available (and usually very expensive) that have a sufficiently high primary intensity and high spatial resolution for imaging with SEMPA.

For a given detector system and sample, ΔP is fixed. With the efficiency of the spin-polarization analyzer at a value around 10^{-4}, it is the product of ΔJ and the dwell time that have to be optimized to obtain the desired accuracy. If dwell times are kept short, we will obtain the specification for the column. The number ΔJ given in the last equation can be expressed by the rate of primary electrons and the secondary electron yield Y. For reasonable values of ΔE_D, 60 to 80% of the true secondaries are used in the spin analyzer. For the further estimation, we take 70%. The secondary electron yield depends strongly on the primary electron energy. It varies monotonically from 0.2 for primary energies of 20 keV [29] to 1 for 3 keV [42]. For the following, we take 0.2, as most of the SEM columns are designed to be used and show best performance (spatial resolution, probe current) at highest energies.

This means we get only $0.7 \times 0.2 = 0.14$ secondary electrons per incoming primary electron. Thus, the primary current required is correspondingly larger by a factor of about seven. Converting from number of electrons to charge ($I = Je$) gives

$$I_{\mathrm{P}}\, t = 7.15 \times 10^{-12}\, C \tag{7.11}$$

to achieve the previously discussed magnetization contrast. The measuring time is limited by experimental constraints, i.e., mechanical stability, vacuum condition, and image size. A dwell time of 10^{-3} seconds gives a time per image of $T = 65$ s (260 s) for an image size of 256×256 pixel (512×512). To achieve the 10% accuracy for Fe, a probe current of about 7 nA (for $Y = 1$, it is $I_{\mathrm{P}} = 1.5$ nA) is required. These numbers are quite high for SEM columns, particularly when the spatial resolution should be high. For dwell times of 10^{-2} sec, the current has to be in the range of 0.7 nA, which means that the time to take an image increases to about 10 min (45 min). This measuring time puts some stronger constraints on the vacuum condition and mechanical stability. If the goal is to resolve fine structures of the magnetic microstructure, the accuracy has to be increased. For 1% uncertainty in spin-polarization measurement, the primary current would have to be raised by a factor of 100. Probe currents of this range are far out of reach when high spatial resolution is required. Dwell times have to be raised and the number of pixels has to be reduced. Line scans are the best approach under such circumstances, which were actually employed in the investigation of domain walls [25,26].

High probe current is at variance with high spatial resolution [48]. Particularly for thermionic guns, a current of nA is already considered high with resolution better than 0.1 μm. The best choice under these prerequisites seems to be the field emission (FE) column. Due to the high brightness of the electron source (called tip), focusing with highest resolution for probe currents in the desired range becomes feasible. The field emission guns offer the possibility of spatial resolution below 10 nm with probe currents in the range of nA [34]. This property of field emission is the reason why most of the spin-SEMs are equipped with such sources [3,5,6,11].

FE guns, however, are not easy to work with. The problems with cold field emission are short-term fluctuations and long-term drift. While the fluctuations do not pose a problem in SEMPA, due to the normalization procedure to obtain the quantity "polarization", the latter problem has to be considered important. Due to contamination of the tip, the emission current drops dramatically around two orders of magnitude on the time scale considered here, i.e., an acquisition time per image in the range of minutes. Hence, the above-mentioned advantage of high resolution and high probe current has to be modified in the sense that it is only true for a very short time after preparation of a clean tip. To bypass that problem, hot field emission is performed, delivering slightly lower resolution but higher stability as the contamination of the tip is prevented [14,34].

Another advantage of field emitter systems is the fact that low energy operation is possible with still reasonably good spatial resolution. This is favorable, as the secondary electron yield increases considerably when the primary energy is reduced. This allows another optimization of the achievable secondary electron rate by tuning the column. A peak in the total secondary electron rate will show up as a compromise of increasing SE yield and decreasing column performance, i.e., probe current, at lower primary energies.

Field emission guns are, however, generally limited to a maximum current that they can deliver. This is different with thermionic emitters. If the resolution is not of primary concern, thermionic guns will be the best choice. They are much easier to handle and give access to faster data acquisition in combination with analog signal processing [29]. The latter condition is not achievable with field emission. The resolution for LaB_6 emitters (thermionic gun) is some 10 nm in the desired current range (nA) [48].

7.2.4 Polarization Vector Analysis

As discussed, SEMPA can measure the magnetization vector. For in-plane magnetization P_x, P_y is measured for every pixel. Instead of displaying images, one can display information as scatter plots [7]. A scatter plot of the vector in the $P_x P_y$ plane is the frequency distribution of the P vector. Any information about the lateral position is dismissed. An example of a scatter plot is given in Fig. 7.7b, derived from the domain image given in Fig. 7.7a, which shows a vortex structure in a small disc (only pixels from inside the disc have been used in the scatter plot). The resulting scatter plot exhibits a ring revealing the uniform distribution of the magnetization vector in all in-plane directions. If the magnetic microstructure exhibits well defined domains, the plot will show a clustering of polarization vectors around the domain magnetization directions [7]. Hence, such plots directly display the symmetry and

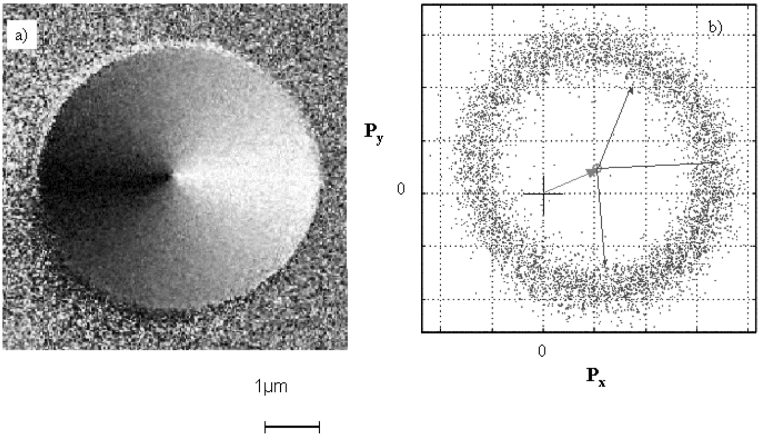

Fig. 7.7. Domain image of a thin film disc and scatter plot of measured polarization vectors. The domain image (**a**) exhibits a vortex structure in a small soft magnetic disc. The scatter diagram (**b**) is created from the two polarization values measured at every spot inside the disc. The cross in the scatter diagram represents the origin, while the *thicker arrow* to the center of the ring gives the vector of apparatus asymmetry. Every dot in the scatter plot represents the polarization doublet obtained at one pixel of the image of the domain structure. Courtesy G. Steierl

the magnetization direction of the domains (i.e., easy axes of magnetization). The center of the ring (Fig. 7.7b) is obviously shifted with respect to the origin. The vector assigned to the displacement of the center of the ring from the origin is the apparatus asymmetry within the plane of polarization detection. A large vector of apparatus asymmetries indicates that the detector system is not well aligned or technical problems of mechanical (alignment) or electrical (detection efficiency, counting electronics, saturation effects) origin exist.

The scatter plot further allows a direct transformation of the domain structure into domain images with full vector information, i.e., the spatial distribution of magnetization vector orientation. Two different situations, can in general occur. First, the polarization is oriented completely parallel to the plane of the detector. In this situation, the complete vector information is contained in the image. The scatter plot will show a symmetry with points equally spaced from the center of a ring like in Fig. 7.7b. The distance between the center of clusters and the asymmetry-corrected origin or the radius of the ring is the absolute value of polarization. The scatter plot yields a very easy way of coding the domain image. A color wheel can be assigned to the in-plane angle directly [29, 49]. The second situation appears when the planes of the polarization detection and magnetization orientation do not coincide. In this situation, the tilting angle can be determined and corrected. If, however, domains exist with magnetization pointing out of the plane of detection, the scatter plot will show clustering at points with different distances to the origin. Scatter points that are farthest away represent in-plane domains and give the absolute value of the polarization. The scatter points that are closer to the origin (corrected for apparatus asymmetry) can be used to determine the tilt angle of the polarization vector. Using a color wheel proposed by Hubert and coworkers [50], the transformation can yield domain images that reflect information about all three components.

7.3 Case Studies

Very different techniques are used to investigate the magnetic microstructures in ferromagnets. All of these techniques have their strengths and drawbacks that make them best suited for the investigation of different aspects of magnetism. In the first section, we will give some examples that show the strengths of spin-SEM, concentrating on ultrathin film systems. The second section will discuss apparent drawbacks of the technique and possible ways around them.

7.3.1 Ultrathin Films

One advantage of SEMPA is its high surface sensitivity, which gives the signal, i.e., polarization, as an average over only a few atomic layers. This fact makes it feasible to investigate systems with thicknesses in the nanometer and sub-nanometer range, i.e., of a few atomic layers only. The technique works in reflection, which puts no limitation on the dimensions of the support of the ultrathin ferromagnet. In particular, that means spin-SEM allows the investigation of ideal systems like single crystal ferromagnets or, utilizing its surface sensitivity, the best thin films one can fabricate by growing them epitaxially on single crystal surfaces. Those well characterized ultrathin films allow for a better and easier interpretation, as the magnetic properties can be correlated with structure and morphology. Another very special feature of ultrathin films is that the magnetization orientation is identical throughout the thickness of the film as long as the thickness is smaller than the characteristic magnetic length λ. The characteristic length is either $\lambda_{\mathrm{K}} = \sqrt{\frac{A}{K}}$ or $\lambda_{\mathrm{ms}} = \sqrt{\frac{A}{2\pi M_{\mathrm{S}}^2}}$, with A the exchange stiffness, K the anisotropy constant, and M_{S} the saturation magnetization, depending on the energy that determines the microstructure, i.e., either the anisotropy or the dipolar energy [50]. The unique situation is that the magnetic microstructure observed at the surface is that of the complete ferromagnet. This makes the interpretation and the setup of the magnetic energy balance straightforward, without the need for assumptions one is forced to make for bulk ferromagnets. A direct correlation between magnetic microstructure and various energy contributions become feasible.

We will first discuss the influence of surface and interface contributions to the magnetic anisotropy of films with perpendicular magnetization. The second section deals with films magnetized in the film plane. In such systems, magneto-static energies due to wall structures are dominant and determine the microstructure. The last subsection is devoted to the exchange coupling across very thin spacer layers.

7.3.2 Films with Perpendicular Magnetization

In films with magnetization perpendicular to the film plane, a competition between two magnetic energies is found. One is the surface/interface anisotropy, which in distinct systems prefers the vertical magnetization orientation. The other is the magneto-static energy. Due to magnetic charges appearing at the surface of a vertically magnetized film, a field is created inside the magnet that is oriented opposite to the sample magnetization. The magnetization is destabilized by its own field, and the system is in a high energy state. In an infinite film, no field is created when the magnetization is lying in the plane. Hence, the in-plane magnetized state has a lower energy with respect to magneto-statics.

While the interface and surface contribution is constant with film thickness, i.e., gives a constant energy per film area, the magneto-static contribution depends on thickness. The latter can be easily visualized as the number of magnetic moments in the internal field (which is constant, as the charges at the interface do not change) increases linearly with thickness. Hence, the related energy per area E^{S} can be given in first-order anisotropy approximation as

$$E^{\mathrm{S}} = K_1^{\mathrm{S}} \sin^2 \Theta - t \left(2\pi\, M_{\mathrm{S}}^2 - K_1^{\mathrm{V}}\right) \sin^2 \Theta \;, \qquad (7.12)$$

using the convention that θ is the angle to the normal and a positive value for K favors vertical magnetization. M_{S} is the saturation magnetization and t the film thickness. A possible volume anisotropy contribution is included (K^{V}) in the formula. In case the surface and interface favors a vertical magnetization, the first expression wins for ultrathin films. The second part becomes dominant with increasing thickness.

As the magneto-static energy is usually larger than K^{V}, the magnetization turns into the film plane, a so-called spin reorientation. This unique behavior in ultrathin films, which gives an easily accessible control parameter, caught the attention of many physicists as soon as perpendicular magnetized films were discovered (for an overview, see [6,51–53], see also Chaps. 1 and 6 in this book).

The Co/Au(111) system [54–56] was the first in which the spin reorientation was studied by means of spatially resolved techniques [33,57]. In the following, we will discuss the results in the framework of the physics of spin reorientation.

The growth of Co on Au(111) was found by no means to be perfect [58]. The cobalt nucleates as double-layer islands at the elbows of the herringbone reconstruction of the Au(111) surface. The islands grow when more material is deposited and finally coalesce. Even at a coverage of seven atomic layers, or monolayers (ML), the film has a granular structure and is rough. The film can be made considerably smoother by heating [55,59]. This smoothing has a very strong effect on the domain structure [59]. One remarkable feature of the domain structure after heating is shown in Fig. 7.8. A sequence of zooms into one particular thickness regime of a wedge-shaped film is displayed. The images show the vertical component of magnetization only. The Co wedge was grown through a mask that yields a Co stripe on the Au(111) single crystal surface. An overview of the domain structure is given in Fig. 7.8a. In the low thickness regime, domains pointing in or out of the film are coded as black and white. At higher thicknesses the contrast diminishes, e.g., the contrast is the same as on the gold substrate. In that part, the magnetization is in the film plane. On the left-hand side, where the film is very thin, domains exist that are similar to those obtained in non-annealed films. This indicates that the annealing cannot wipe out the roughness in the low coverage regime and pinning of domains [6] is still dominant. Interesting, however, is the reappearance of small domains at higher thicknesses just before the magnetization flips into the film plane. Here, the domains become even smaller than in the regime of low thicknesses, which is demonstrated by the zooms into that regime (Fig. 7.8b,c). The domain size seems to collapse upon thickness increase. The origin of this behavior is purely magnetic. The gain of magneto-static energy lets the film break up into small domains. The gain in total energy, however, is achieved at the expense of domain wall energy.

The energy balance of a thin ferromagnet with stripe domains was theoretically worked out a long time ago [60], while an analytical approximation for the semi-convergent series given in [60] was published only a few years ago [61,62]. With the analytical solution for the magneto-static energy, the domain size D can be given as [61]

$$D = x\,t\,\exp\left(\frac{\sigma_{\mathrm{W}}}{4\,t\,M_{\mathrm{S}}^{2}}\right)\,, \tag{7.13}$$

with t as thickness and σ_{W} as domain wall energy. The same formula is obtained for stripe and checkerboard patterns [61]. The geometry factor x accounts for the two different geometries [61]. The analytical solution allows one to fit the thickness-dependent domain size of the SEMPA images. The influence of the competing energies is included in the ansatz for the Bloch wall energy. An effective anisotropy

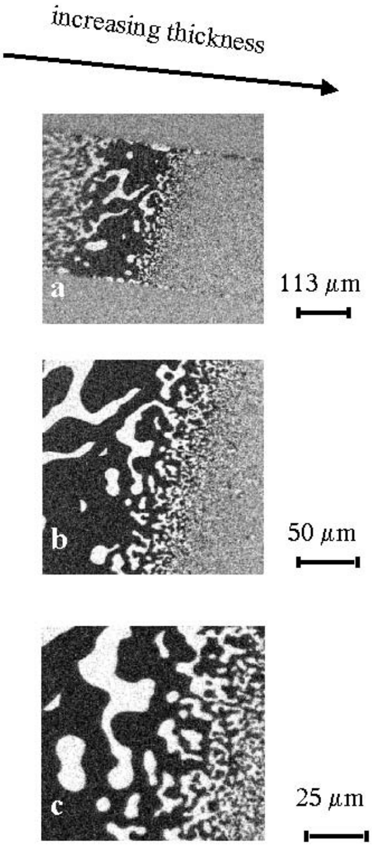

Fig. 7.8. Domain structure in a Co wedge on Au(111). The thickness increases from left to right. The pictures give the vertical component of magnetization. Black/white means that the magnetization points into/out of the plane of drawing. Gray indicates that no vertical component exists. The magnetization is either orientated in the film plane or zero. (**a**) shows a survey displaying the Co stripe and parts of the Au(111) surface. At the low thickness side, domains exist that are determined by film morphology. (**b**) and (**c**) are zooms into the range where the vertical magnetization is fading away. A collapse of the domain size is found

constant has to be introduced. The Bloch wall energy σ_W is thus

$$\sigma_W = 4\sqrt{A\,K_{\mathrm{eff}}}\,, \tag{7.14}$$

with A the exchange stiffness and the effective anisotropy K_{eff} taken from above, i.e.,

$$K_{\mathrm{eff}} = \frac{K_1^S}{t} + K_1^V - 2\pi\,M_S^2\,. \tag{7.15}$$

Taking the literature value for the first order volume (or bulk) anisotropy constant of hcp-Co, the experimental results can be fitted using the first order surface anisotropy as the only fit parameter. The result is $K_1^S = 0.83\,\mathrm{erg/cm^2}$ (checkerboard), which stands for the sum of the two interface anisotropies involved, i.e., the surface and the Au-Co interface [59]. The value fits quite nicely into the span of published interface anisotropies for Co/Au(111) that have been obtained by other methods [52].

With the value for K_1^S we can calculate the magnetic energies at the thickness where the smallest domains appear in Fig. 7.8 (domain size $\sim$ 500 nm, $t \sim 4.75$ ML). With the formula given in [61] we obtain for that domain size a gain in magneto-static energy of 1.6% of the total magneto-static energy, while for that thickness the expense of energy due to domain wall creation is 0.64% of the total magneto-static energy. As the gain in magneto-static energy is highest where the domains are smallest, it will be smaller in the lower thickness regime. We thus may conclude that the concept of an effective anisotropy, which takes as a correction $2\pi M_S^2$ for the magneto-static energy, is a very good approximation. The error margin of this approximation is below 1.6% for all thicknesses considered in the fit. This estimation further demonstrates that the speculation that magneto-static interactions throughout the wedge might change the physics [6] is unjustified on the much larger scales of the typical slopes of the wedges.

The effective anisotropy at the thickness of collapsing vertically magnetized domains is $\sim$ 10% of the total magneto-static energy. With that effective anisotropy one can calculate the domain wall width. The resulting wall width is in the range of 1/10 of the domain size, i.e., $30-50\,\mathrm{nm}$. This ratio of domain wall width to domain size is within the range of the validity of the approximation [61, 62]. This gives another justification for the fit.

The non-zero effective anisotropy poses the question at what thickness the effective anisotropy is actually vanishing. A straightforward calculation using the above value for the surface/interface anisotropy reveals that this should happen at a thickness of 5 ML, i.e., the film thickness at which the first order anisotropy is canceled by the magneto-static energy. In the experiments, this thickness turned out to be very special. At this thickness the first in-plane magnetized domains appear [63]. Moreover, it was found that a magnetic field applied perpendicular to the film drives the film into a single domain state (except of the very thin film region) with a borderline at about 5 ML [63]. This means that upon applying a field, a state of vertical magnetization is created that spans a larger thickness range than the multi-domain vertical state. The latter represents the equilibrium or, more precisely, a state with lower energy, as the estimation of the involved energies has revealed. The former state, however, gives the total thickness range of possible vertical magnetization. Hence, as even the external fields cannot push the vertical magnetization to higher thicknesses, the upper borderline (at 5 ML) must represent the line of absolute stability above which the in-plane magnetization becomes the only stable state. In other words, we may conclude that the experiments with fields confirm the calculated borderline (or thickness) of first order anisotropy cancellation. It must be emphasized that the calculations are based on the outcome of the magnetic microstructure analysis of the state of equilibrium, while the single borderline appears after magnetizing procedures.

The influence of the magnetic field and the meaning of the appearing borderline can be utilized to study the influence of the interface properties on covering the

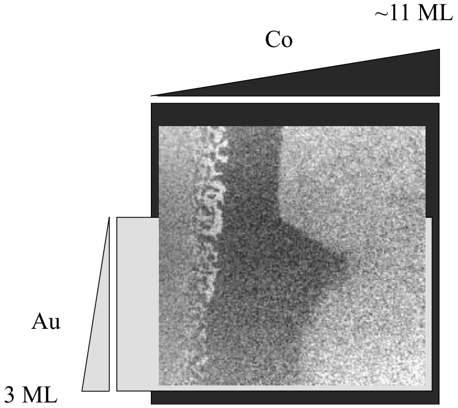

Fig. 7.9. Domain structure in Co on Au(111) partially covered by Au. The vertically magnetized domains are displayed. A double-wedge structure has been fabricated with Co thickness increasing from left to right. The thickness of the Au capping layer increases from top to bottom starting in the upper half of the image. A magnetic field has been applied vertically prior to imaging. The degrading image quality in the lower part is due to the increasing Au coverage that reduces the polarization of the secondaries

surface by nonmagnetic material. Figure 7.9 shows a double-wedge experiment. On a Co wedge a Au wedge was grown. The gradients in thickness are perpendicular to each other in the two wedges. The film was magnetized in a vertical field. At low thickness, domains persist due to the roughness in the film. In the thicker range, the film is driven into the single domain state (dark gray) by the field. A sharp borderline appears where the magnetization turns into the film plane (light gray). The borderline is shifted to higher Co thicknesses as soon as the Co is covered by Au, which means that the interface anisotropy is becoming stronger. In the sub-monolayer Au coverage, a steep increase is found that indicates how sensitively the surface and interface anisotropy depends on coverage (see also Chap. 6). Similar behavior has also been found due to carbon contamination [64]. The extreme sensitivity of film anisotropy on the condition of the interface and surface is most likely responsible for the large span of reorientation thicknesses or interface anisotropies published for the different systems. The behavior of the perpendicular magnetic anisotropy on coverage has been extensively studied [65–67]. The significance of the SEMPA image, however, is that it represents a snapshot of the whole span of coverage with infinitely small increments of changes, while conditions of growth and preparation are identical.

All experiments found an offset between the thickness where the perpendicular domains disappear and the thickness where in-plane domains emerge. The field experiments reveal that between these two borderlines, or lines of discontinuities, the films can exhibit two different states of magnetization, i.e., meta-stability. Meta-stability will only exist if different states of magnetization have a local minimum in their angle-dependent free energy at the same value of the driving parameter, here the thickness [63]. Such a coexistence of states was proposed for ferromagnets with uniaxial anisotropy in which the first order anisotropy becomes weak and the second order anisotropy contribution comes into play. A phase diagram was suggested describing the ranges of stability in the anisotropy space [68]. Under the condition that the second order anisotropy depends on thickness in the same way as the first order, a thickness variation is represented by a straight line in the phase diagram in anisotropy space [69]. This fact allows the direct assignment of the two lines of discontinuity appearing in the domain images to the two borderlines of the state of coexisting phases. The corresponding thicknesses can in turn be used to calculate the second order surface anisotropy with high precision [63].

The remaining question from the SEMPA investigation is about the origin of the lines of discontinuity. In the experiment, these lines are visible due to a reduction in signal in the range of coexistence. A reduced remanence was also reported in early investigations of the reorientation in low-temperature grown Fe/Cu(001) [70, 71]. The non-spatial resolving experiment was resumed by Allenspach performing spin-SEM investigations [72]. It was clearly demonstrated that the range in thickness and temperature with reduction of remanence was not as large as that found in the first studies. This was attributed to the fact that domains were not completely erased in the previous studies [6]. Still, the very careful investigation revealed a reduction in signal in a very small thickness and temperature range. This result is actually equivalent to the finding in the Co/Au(111). Allenspach found small in-plane domains that were assumed to be responsible for the reduction. Very small in-plane domains were found also in spin-polarized LEEM experiments on Co/Au(111) (see also Chap. 6) [73]. Hence, we might expect the same to happen in Co/Au(111), reducing the signal as in the case of Fe/Cu001) [6]. In that particular range of anisotropy values there is apparently a possibility for domains with both orientation of magnetization (vertical and in-plane) to coexist. The latter scenario has been theoretically confirmed and worked out by Monte-Carlo simulations [74]. The simulation reveals that the size of the different domains depends on the depth of the minima for the different magnetization orientations [74].

The above examples demonstrate how the magnetic microstructure can be used to extract magnetic quantities by a careful examination of the domain structure. In experiments on thickness-dependent properties, the slope of the wedges allows for extremely high thickness resolution. The variation of the slope of the wedge makes it feasible to separate thickness-dependent properties, morphology-determined behavior, and micromagnetic behavior. The examples given here are considered ideal systems as the behavior, in particular the spin reorientation, is solely driven by magnetic properties. The findings prove that assumption true. More often, the spin reorientation is a secondary effect driven by changes in structure or electronic properties. One of the most widely studied thin film ferromagnets, room-temperature-grown Fe/Cu(001) [75], belongs to this class of systems. Here, the spin reorientation is accompanied by a structural change [76]. Most likely the structural change drives the change of magnetization orientation. Those systems cannot be treated solely on magnetic grounds. In such films, however, the magnetic properties are an extremely sensitive probe for resolving the transition of structural or electronic origin. Hence, the magnetic investigation can be utilized to study e.g. structural phase transitions with extremely high accuracy. Such spatially resolved experiments have not been performed yet.

7.3.3 Films with In-Plane Magnetization

In this paragraph, we deal with ultrathin films with magnetic anisotropy that favors in-plane magnetization or systems with very small magnetic anisotropy. From the micromagnetic point of view, such films seem to be by far not as interesting as systems with perpendicular magnetization [6]. This is due to the fact that for infinitely large films, i.e., with lateral dimensions much larger than the thickness, the state of lowest energy is the single domain state since the magneto-static energy of a mono-domain with in-plane magnetization is almost zero [77, 78]. So there is no driving force for the creation of domains, as the domain wall energy, which has to be expended, is not balanced by a gain in anisotropy energy. Actually, it was found in the ultrathin films that the as-grown state is single domain [79]. The magneto-static energy, however, is exactly zero only in the case of infinitely extended films. With finite size the magnetic poles created at the edge of the film are responsible for a local field that can generate small domains just at the edges, called edge domains [31, 79]. Edge domains were also observed in thick films, i.e., in films with thickness up to 1 μm, some time ago [80]. In spite of the fact that the mono-domain state is the state of lowest energy, domains could be created in ultrathin films and turn out to be stable [32]. The domain pattern is characterized by a very irregular structure. In spite of a reasonably strong fourfold magnetic anisotropy of the Co/Cu(001) films [81], the domain structure revealed no remnants of this symmetry in contrast to common experience. The same was also found in uniaxial in-plane magnetized films of Co/Cu(1 1 13) [82]. In brief, the reason for that special feature of the domain structure are the domain walls, which are Néel walls [83]. A Néel wall prevents surface charges while volume charges are created, because in the wall the magnetization rotates within the film plane. The walls have a narrow core and long-ranging tails that are created by the volume charges on both sides of the wall. This has been found for films with very small magnetic anisotropy [84]. The tails have been described theoretically by a logarithmic dependence [85, 86]. Qualitatively, the same wall profiles have been observed in the ultrathin films in spite of the magnetic anisotropy [87]. Due to the wall tailing, a strong interaction of walls acts in the ultrathin film that creates the irregular domain structure. While the domain structure is affected, the interaction also changes the wall profile, which causes difficulties in determining the unperturbed profile, i.e., particularly the tail.

Although the domain structure is not the state of lowest energy the domain structure is stable. It is not clear which mechanism stabilizes the domains. It is not the influence of imperfections that have been shown to be of minor or even no importance [6, 79]. The understanding of the domain structures, however, would yield more information about magnetic or structural properties. Simulations are difficult due to computation limitations, as large sample sizes have to be considered. Yet, the understanding of the main features of the microstructure will become an important

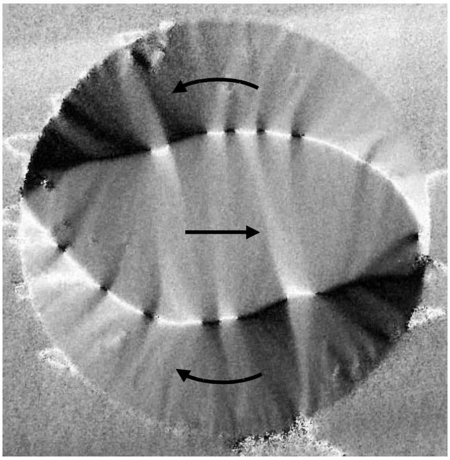

Fig. 7.10. SEMPA image of a Co disc (polycrystalline) with a diameter of 10 μm. The image gives the angle distribution of magnetization within the film plane. The magnetization orientation has been calculated from the measurements of two orthogonal magnetization components. The resulting orientation is coded in gray. For the sake of simplicity the *arrows* are drawn that reveal the flow of the magnetic flux. The domain walls are cross-tie walls which have to be expected for the thickness of the structures

issue as such films are considered for the use in future storage or (hybrid) electronic devices.

Complex structures of domain walls are known for thicker films of soft magnetic materials, i.e., cross-tie walls (see also Chap. 11) [88]. Cross-tie walls are created in certain thickness ranges when the wall structure switches from Néel- to Bloch-like walls. Although such walls have large lateral extensions, they are better understood [89–91]. They consist of legs with Néel-type character and Bloch-lines that transform to Bloch-walls upon thickness increase. Cross-tie walls can be seen in the SEMPA image shown in Fig. 7.10. The thin film structure (thickness = 40 nm) is made from polycrystalline Co, which has a low magnetic anisotropy. Due to its finite dimensions, the magneto-static energy overcomes the anisotropy energy and determines the domain structure counterbalanced by the exchange energy. The minimization of the magneto-static energy lets the system prevent any pole at the structure edges, which creates a so-called flux closure structure. Following the *arrows* in the image it becomes obvious how the magnetization is closed in itself. The cross-tie walls that are formed extend in some cases throughout large parts of the structure. A detail of the wall is shown in Fig. 7.11 along with a sketch of the cross-tie. Two different Bloch lines appear in a regular sequence. One is the center of a swirl, while the second type appears at points where the Néel-type legs merge into the wall center. The spatial resolution for magnetic structure in this image is less than 30 nm [92]. Nonetheless the structure of the Bloch lines is not resolved. The Bloch lines are singularities where, for symmetry reasons, the magnetization is pointing out of the

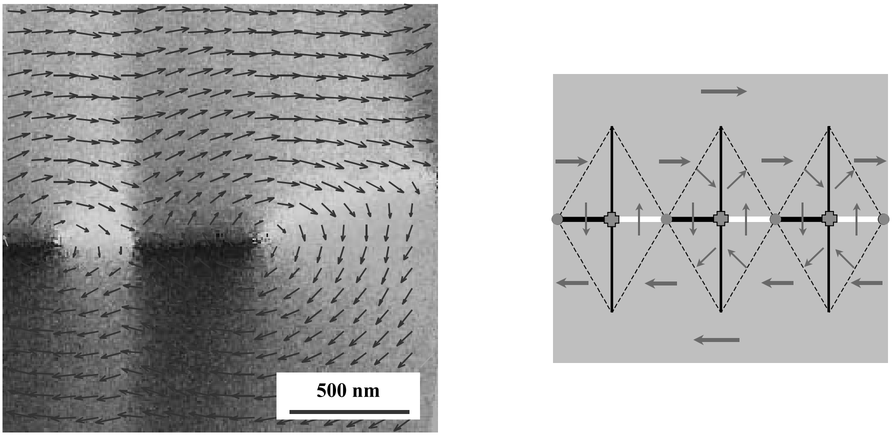

Fig. 7.11. Detail from Fig. 7.10 showing the fine structure of the cross-tie. The *arrows* given in the domain image on the left-hand side are the results of the SEMPA investigation. A sketch of the cross-tie wall is given on the right-hand side [50]

film plane [50]. The fine-structure has not yet been experimentally resolved (see also Chap. 11).

7.3.4 Exchange Coupled Films

The discovery of antiferromagnetic coupling in Fe/Cr/Fe structures and of the associated giant magnetoresistance (GMR) effects was a milestone and triggered an explosive growth in the field of ultrathin magnetic films [93, 94]. RKKY-type oscillatory exchange coupling was soon found in many systems with nonmagnetic (paramagnetic) spacer layers [95]. In a very short time these systems found their way into magnetic devices. Here, we will concentrate on the unique contributions made by SEMPA. In a series of studies by the NIST group, various spacer layer materials were investigated: Cr [96–98], Ag [99, 100], Au [101, 102], and Mn [103, 104]. The use of wedged interlayers, Fe whiskers as substrates, and the ability of SEMPA to directly measure the magnetization direction with high spatial resolution revealed many of the details and intricacies of the exchange coupling mechanisms. The Fe whiskers provide exceptionally smooth surfaces compared with ordinary single crystal substrates. The classical example of Fe/Cr/Fe has contributed most to our knowledge. The epitaxy of this system is of very good quality and, therefore, shows the various coupling effects most clearly. Furthermore, the SDW structure of Cr adds another dimension to the problem.

The surface sensitivity of SEMPA allows the use of ultrathin top Fe layers, which are typically 2 nm thick. On the wedged samples, the oscillatory coupling is directly visible in the SEMPA images. Short and long periods are observed in the Fe/Cr/Fe system, depending on growth conditions. Only samples with an elevated growth temperature show the short period (two atomic layer) oscillations, while for the low-temperature-grown samples, the short period oscillations are absent due to interface roughness. This study led to detailed investigations of the Fe/Cr growth. Combined SEMPA and STM showed the importance of interface alloying [97,98].

SEMPA studies on Fe/Cr/Fe, in which the polarization vector was measured, revealed the presence of perpendicular (biquadratic) coupling. This was found primarily at interlayer thicknesses where the bilinear (collinear) coupling was small. In this case, biquadratic coupling can even become dominant. Similar effects were seen in other systems and perpendicular coupling is now a rather common phenomenon associated with interface roughness. In the most general case, the magnetic coupling can result in non-collinear alignment, i.e., the magnetization directions are at intermediate angles. This has been studied in detail in the Fe/Mn/Fe system [103,104]. A disadvantage of SEMPA is that coupling strengths cannot be measured directly, since SEMPA cannot be applied in a magnetic field (but see later). The NIST group combined SEMPA studies with MOKE [102].

Antiferromagnetic (AF) exchange coupling is, of course, not restricted to AF interlayer materials (like Cr or Mn). However, AF order is crucial in a different context. The phenomenon is now known as exchange bias and has been known for a long time [105]. The effect consists of a shift of the hysteresis loop of a ferromagnetic (FM) layer in a field-cooled AF/FM film structure. The AF layer pins the FM magnetization. It has been clear from the beginning that this must be due to the interface magnetic structure, but details have not been worked out. There has been a growing interest in this field. Exchange biasing is widely used in layered magnetic devices. For a recent review of exchange biasing see, e.g., [106]. Until recently, there was no experimental probe available of AF order at surfaces or interfaces (see also Chaps. 2 and 9). Since SEMPA requires a net spin polarization, it is not sensitive to AF order. There is, however, one situation where SEMPA can be applied to AF systems. When the AF order consists of layer-by-layer alternating magnetic moments there will be a net spin-polarization signal due to the surface sensitivity. This was first demonstrated for growth of Cr on Fe(100) in spin polarized electron scattering experiments and also for Mn [107,108]. This case does not even require spatially resolved measurements as long as the surface layer has a macroscopic net magnetic moment. The NIST group showed the oscillating magnetization of Cr surface, grown as a wedge on Fe whiskers [109]. In principle, one could use this to extract surface moments [110]. However, there are many parameters that enter into this model. So it seems rather difficult to extract reliable quantitative information [111].

Two recent SEMPA studies deal with the magnetic structure of FM layers exchange coupled to AF materials, namely ultrathin, Fe films on Cr(100) [12] and NiO(100) [112]. Temperature dependent SEMPA images of 2 nm Fe on Cr(100) are shown in Fig. 7.12. At elevated temperature (slightly above RT), the Fe film can be saturated showing a single domain state in remanence. This is shown in the top panel of Fig. 7.12. When the temperature is lowered, a spin reorientation occurs. The Fe moments show a tendency to turn toward the perpendicular (still in-plane) direction.

However, this is not a uniform rotation, but strong variations of the local turn angle on the 10 micron scale exist (center panels of Fig. 7.12). The turning is attributed to biquadratic coupling due to frustration because of atomic steps [113–115]. The

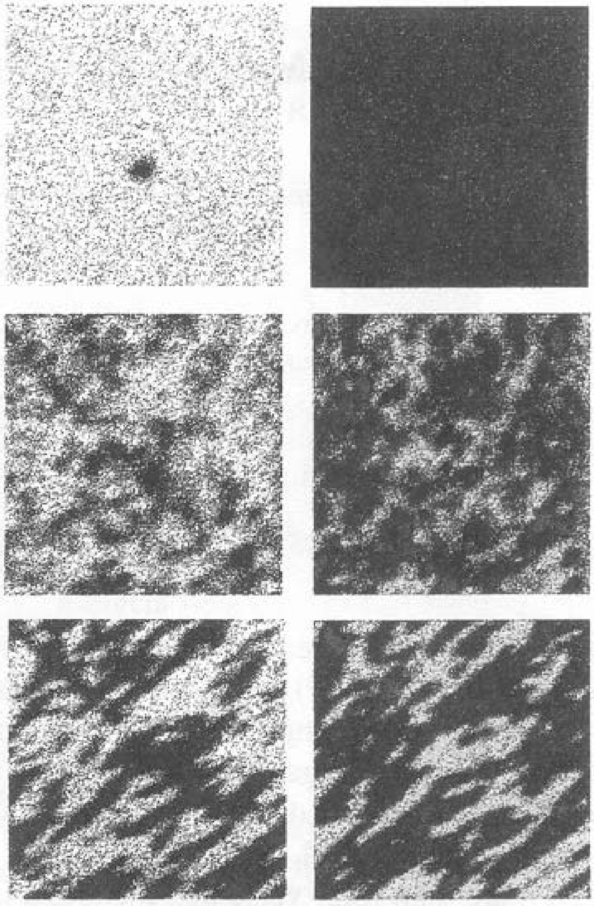

Fig. 7.12. Temperature-dependent images of 2 nm Fe on Cr(100). *Top:* above RT; single domain state after magnetization. *Center:* temperature lowered to about 100 K. *Bottom:* warmed to slightly above room temperature. The *left* and *right columns* show images of the two in-plane magnetization directions, respectively. The image size is about 70 μm

spatially varying magnetization angle is due to varying step densities on this length scale [116].

One has to remember that terrace widths are on the tens of nanometer scale, while the magnetization varies on the micron scale, thus about a hundred times larger. Thus, one is dealing with average step densities. Upon warming to above the Cr ordering temperature, the driving force on the Fe magnetization disappears and the Fe film forms conventional domains with the magnetization pointing in the easy directions. This is shown in the lower panel of Fig. 7.12.

A SEMPA image of 0.9 nm Fe on NiO(100) is shown in Fig. 7.13 [112]. Comparing the Fe magnetization directions with the expected NiO(100) surface spin

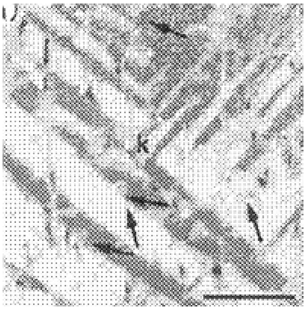

Fig. 7.13. Magnetic domains in 0.9 nm Fe on Ni(100). Image size is 70 μm (after [112])

orientation, it was concluded that a near-perpendicular coupling exists. Of course, it would be highly interesting in the future to determine both the directions of the AF moments (e.g., by linear dichroism measurements) and the FM moments at the same time.

7.3.5 Decoration Technique

The high surface sensitivity of SEMPA is often cited as a major problem that limits the application of the technique to ideal systems. "Ideal" is meant in the sense that the surface of the ferromagnet has to be prepared, i.e., cleaned in-situ before imaging, or, in case of thin films, that the films have to be fabricated in or transferred under UHV conditions into the microscope. In particular, investigations of systems and devices developed for commercial applications having undergone several steps of preparation seem to be inaccessible with SEMPA. This problem has been recognized and discussed since the first realization of the spin-SEM. In the very early stages of the technique, an elegant idea was put forward to overcome that problem. It was suggested to create a fresh and clean surface by depositing a very thin layer of iron on top of the sample. If the Fe layer is kept thin compared to the system under investigation, the film will not alter the magnetic properties while mirroring the domain structure. This decoration technique was successfully proven [117]. It was speculated that the cloning of the surface microstructure is due to the exchange coupling of the adlayer and the ferromagnet, though this has not yet been proven. The consequences of this idea for SEMPA investigations are manifold. First, the trick can be used to enhance contrast at least up to the maximum value, i.e., that of Fe [27, 118]. Secondly, it widens the field of application of SEMPA to the whole class of ferromagnetic materials. While nonitinerant ferromagnets can be investigated [119], it also gives access to insulating ferromagnetic materials. Finally, the decoration technique makes the quality of the surface less important and the investigation of nearly all kinds of samples becomes feasible. An example of the latter situation is given in Fig. 7.14. The thin film structures are fabricated by lithographical methods. After lithography, the surface of the sample is strongly contaminated. Moreover, as can be seen from the topographical image, remnants of the structuring process are randomly spread over the surface. In principle,

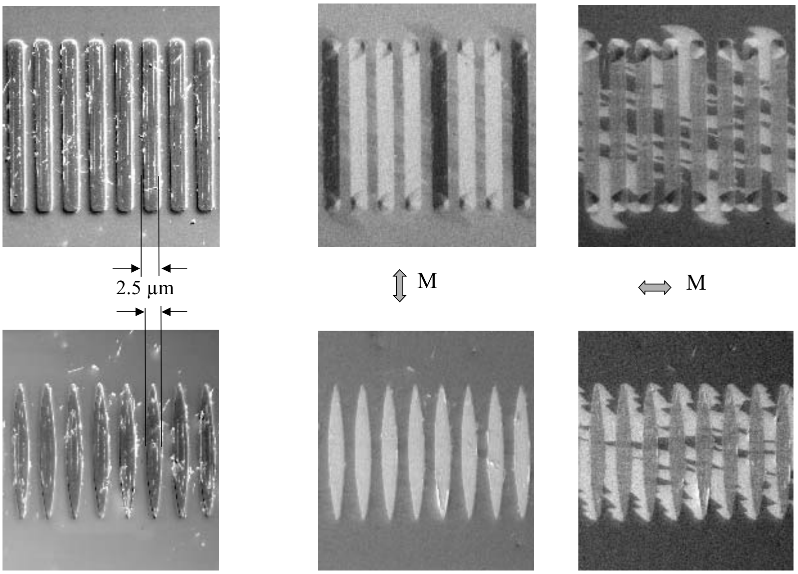

Fig. 7.14. Permalloy thin film structures. The structures were fabricated by means of e-beam lithography. The topography is displayed on the left-hand side. The images at the center and on the right-hand side show the magnetic microstructure obtained in two perpendicular in-plane directions of magnetization. All images in one line were taken simultaneously. Prior to imaging with SEMPA, the sample was covered by an iron film of about 10 monolayers in thickness. The component of magnetization along the horizontal direction (right-hand side) exhibits domains that are induced by the stray fields of the structures

that makes the study in spin-SEM impossible, since the secondary electrons created in the nonmagnetic contamination layer are not spin polarized. Even general SEM becomes difficult due to charging. The topography image in Fig. 7.14 (left-hand side) reveals that some areas are still charging up although the surface has been covered by roughly 10 monolayers of Fe. The right-hand side shows the magnetic microstructure obtained by two perpendicular in-plane components of magnetization [92]. Both images were taken simultaneously. Obviously, a magnetic microstructure is attained. The bars seem to prefer the orientation of magnetization along the long axis. They have been magnetized in a field parallel to the long axis of the bars. While the bars with pointed ends are all magnetized in the same direction, the ones with flat ends are not. A closer look reveals that at the ends of the rectangular bars closure or vortex structures appear that were also found in the so-called acicular structures by Lorentz-Microscopy [120, 121]. Hence, from the equivalence one can deduce that the domain structure of Fig. 7.14 is that of the underlying ferromagnet, which is determined by its morphology although the structures are covered by Fe. In other words, the magnetic microstructure in the Fe layer reflects the domain pattern of the soft magnetic bars.

The thin ferromagnetic layer imparts even more information about the system. The image achieved with the second component of magnetization reveals a magnetic structure in the thin film in the region where there is no magnetic structure beneath. Parts of this structure, particularly above and below the bars, reflect the stray field distribution caused by the ferromagnetic structures. During deposition, the Fe atoms are aligned in the stray fields of the structure and form domains around the structures. The Fe film (at least outside the structures) seems to exhibit a uniaxial anisotropy, which follows from the fact that any domain structure is missing in the vertical, in-plane component. Only the horizontal, in-plane component (probably the easy axis) shows domains. Particularly, the left-right asymmetry at the bottom and top of the oppositely magnetized flat-ended bars are created by stray fields. Without understanding all the details, which would require a sophisticated simulation, one can immediately deduce that the structure at the flat end of the bars does not completely terminate the magnetic flux. Magnetic poles still exist that cause the stray field and its characteristic traces in the film adjacent to the structures. A similar situation explains the domain structure in the film close to the bars with pointed ends. The stray fields are similar for all structures that cause the black/white contrast to appear in a regular left/right sequence.

The two effects determining the domain structure in the film are (a) the reflection of the domain structure of underlying magnetic material and (b) the effect of the stray fields. In this investigation, the film magnetic properties can also be identified, i.e., the films behave uniaxially with an easy axis perpendicular to the orientation of the structures. That fact poses the question for the film properties on top of the magnetic structures. Either it is the same and we have to postulate a coupling of the film to the structure that is stronger than the anisotropy, or the structural and magnetic properties are different on the substrate and the magnetic structure. The question has not been solved, since the sample surface is not very well characterized. Assuming a similar strongly contaminated surface on the whole sample, one might interpret the finding as an indication for exchange coupling between the two ferromagnets.

7.3.6 Imaging in Magnetic Fields

It is commonly stated as a disadvantage of SEMPA that it is incompatible with external fields. In fact, that statement is not generally applicable, since the response to a magnetic field does not necessarily yield more information than what can be extracted from the magnetic microstructure. The only problem is to understand the microstructure and make appropriate calculations, which is often a formidable task. The modeling then reveals the magnetic properties involved. Hence, the imaging in an in-situ field is not always of general importance. That situation has changed recently as nanomagnets become a big issue in research and development. Particularly, the application of nanomagnets in new devices puts the spatially resolved investigations of magnetic reversal into focus. In that research field, the spatial resolution is necessary to attain the response of the low-dimensional structure to the magnetic field. This trend changes the situation and the demand for the combination of SEMPA, with its power of spatial resolution, with external fields is reasonably founded.

What are the problems when using a magnetic field in SEMPA? First, electron beams are deflected in magnetic fields, and complicated steering and corrections are necessary. The second problem is spin precession, which destroys, or at least changes, the information that is used in spin-SEM. Both effects can be reduced to acceptable limits when the impact of the field on the electrons is kept to a low level either by small fields or small field extensions. The former situation was realized using fields up to $800-1200\,\text{A/m}$ $(10-15\,\text{Oe})$ [36, 118]. While in vertical fields the problems are very low because the field is along the direction of electron motion [36], the use of in-plane fields is more delicate [118].

The second approach, i.e., utilizing very localized magnetic fields, has been realized recently [122]. For the SEMPA investigation, a small-scale yoke has been designed that can be positioned as close as $10\,\mu\text{m}$ to the film surface. The yoke has a gap of $\sim 100\,\mu\text{m}$, and the pole pieces have a thickness of $100\,\mu\text{m}$. Magnetic fields up to $\sim 15\,000\,\text{A/m}(\sim 185\,\text{Oe})$ can be applied, which could be determined by measuring the deflection of the primary beam running through the field [122]. The field direction is mainly parallel to the sample surface. The primary beam, as well as the secondary electron beam move through the gap. This setup was successfully used to study the switching of a permalloy microstructure. A small sequence of the field-dependent domain structure is shown in Fig. 7.15. The magnetic field direction is given by the arrow, while the field strength is given at the corresponding domain image. Wall movement is found in low fields, while in high fields, domains are

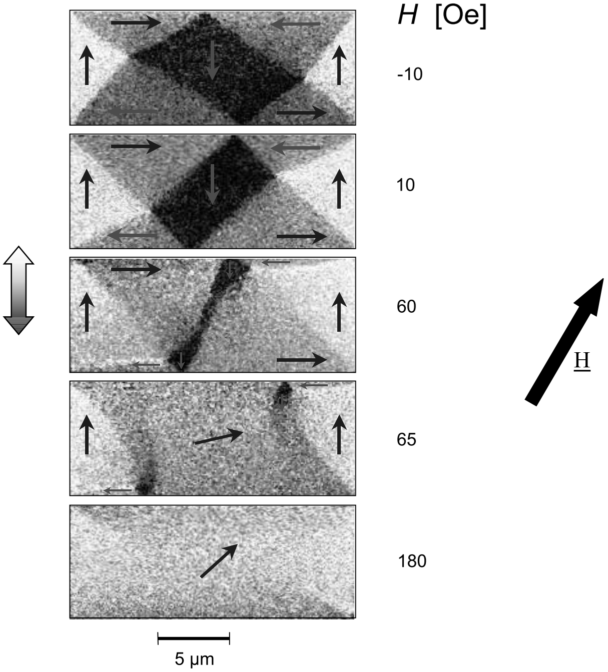

Fig. 7.15. Permalloy thin film structure. The SEMPA images are taken while the fields are applied. The field direction is given by the *arrow*, while the strength (in Oe) is indicated at the individual domain pictures

irreversibly annihilated and finally the magnetization rotates. Very similar behavior is known from literature and textbooks [50, 120].

The examples given in this paragraph demonstrate the potential of SEMPA even in applications where it was commonly believed that SEMPA could not work successfully. The few examples prove the applicability of SEMPA investigations in the new field of applied research, i.e., the device development based on nanostructures called "Spintronics."

7.4 Conclusions

Spin-SEM provides a powerful tool for the investigation of magnetic domain structures in ultrathin films. The very unique feature is that the magnetization orientation is measured with high spatial resolution. This has been successfully applied in studying the internal structure of domain walls, spin-reorientation in ultrathin films, and exchange coupling in films. Further developments are still under progress, pushing the limits of spatial resolution into the range of a few nanometers. A big step forward would be achieved if spin-polarization analyzers with higher sensitivity were available. Preparation techniques have been developed that allow the investigation of nearly all kinds of samples with SEMPA. The first in-field imaging has been successfully demonstrated.

Acknowledgement. HPO would like to thank G. Steierl and J. Kirschner for allowing their images to be included prior to publication. Support from the "Bundesministerium für Bildung und Forschung" (No. 13N7331/4) is gratefully acknowledged. HH gratefully acknowledges research support from the NSF. The SEMPA project was also supported by the Sony Research Center.

References

1. R.J. Celotta and D.T. Pierce in: Microbeam Analysis-1982, K.F.J. Heinrich (ed.), San Francisco Press, p. 469.
2. J. Kirschner, Scanning Electron Microsc. **III**, 1179 (1984).
3. K. Koike and K. Hayakawa, Jpn. J. Appl. Phys. **23**, L187 (1984).
4. J. Unguris, G. Hembree, R.J. Cellota, and D.T. Pierce, J. Microscopy **139**, RP1 (1985).
5. H.P. Oepen and J. Kirschner, Scanning Micros. **5**, 1 (1991).
6. R. Allenspach, J. Magn. Magn. Mater. **129**, 160 (1994).
7. T. VanZandt, R. Browning, C.R. Helms, H. Poppa, and M. Landolt, Rev. Sci. Instrum. **60**, 3430 (1989).
8. E.A. Seddon, Y.B. Xu, D. Greig, J.R.M. Wardell, D. Rubio-Temprano, and M. Hardiman, J. Appl. Phys. **81**, 4063 (1997).
9. Y. Iwasaki, M. Takiguchi, and K. Bessho, J. Appl. Phys. **81**, 5021 (1997).
10. Y. Lee, A.R. Koymen, and M.J. Haji-Sheikh, Appl. Phys. Lett. **72**, 851 (1998).
11. C. Stamm, F. Marty, A. Vaterlaus, V. Weich, S. Egger, U. Maier, U. Ramsperger, H. Fuhrmann, and D. Pescia, Science **282**, 449 (1998).

12. H. Hopster, Phys. Rev. Lett. **83**, 1227 (1999).
13. J. Barnes, L. Mei, B.M. Lairson, and F.B. Dunning, Rev. Sci. Instrum. **70**, 246 (1999).
14. G. Steierl, H.P. Oepen, and J. Kirschner, to be published.
15. J. Kessler: "Polarized Electrons", 2nd edn., Springer, Berlin, 1985.
16. T.J. Gay and F.B. Dunning, Rev. Sci. Instrum. **63**, 1635 (1992).
17. G.C. Burnett, T.J. Monroe, and F.B. Dunning, Rev. Sci. Instrum. **65**, 1893 (1994).
18. J. Unguris, D.T. Pierce, and R.J. Cellota, Rev. Sci. Instrum. **57**, 1314 (1986)
19. M.R. Scheinfein, D.T. Pierce, J. Unguris, J.J. McClelland, R.J. Celotta, and M.H. Kelley, Rev. Sci. Instrum. **60**, 1 (1989).
20. J. Kirschner and R. Feder, Phys. Rev. Lett. **42**, 1008 (1979).
21. J. Kirschner: "Polarized Electrons at Surfaces", Springer, Berlin, 1985.
22. G.G. Hembree, J. Unguris, R.J. Celotta, and D.T. Pierce, Scanning Microsc. Intern. Suppl. **1**, 229 (1987).
23. K. Koike, H. Matsuyama, and K. Hayakawa, Scanning Microsc. Intern. Suppl. **1**, 241 (1987).
24. K. Koike, H. Matsuyama, K. Hayakawa, K. Mitsuoka, S. Narishige, Y. Sugita, K. Shiiki, and C. Saka, Appl. Phys. Let. **49**, 980 (1986).
25. H.P. Oepen and J. Kirschner, Phys. Rev. Lett. **62**, 819 (1989).
26. M.R. Scheinfein, J. Unguris, R.J. Celotta, and D.T. Pierce, Phys. Rev. Lett. **63**, 668 (1989).
27. J. Unguris, to be published in: "Magnetic Imaging and Its Application to Materials", see http://physics.nist.gov/Divisions/Div841/Gp3/epg_files/pub.html.
28. J. Kirschner and S. Suga, Solid State Commun. **64**, 997 (1987).
29. M.R. Scheinfein, J. Unguris, M.H. Kelley, and R.J. Celotta, Rev. Sci. Instrum. **61**, 2501 (1990).
30. T. Kohashi, H. Matsuyama, and K. Koike, Rev. Sci. Instrum. **66**, 5537 (1995).
31. J.L. Robins, R.J. Celotta, J. Unguris, D.T. Pierce, B.T. Jonker, and G.A. Prinz, Appl. Phys. Lett. **52**, 1918 (1988).
32. H.P. Oepen, M. Benning, H. Ibach, C.M. Schneider, and J. Kirschner, J. Magn. Magn. Mater. **86**, L137 (1990).
33. R. Allenspach, M. Stampanoni, and A. Bischof, Phys. Rev. Lett. **65**, 3344 (1990).
34. H. Matsuyama and K. Koike, J. Electron. Microsc. **43**, 157 (1994).
35. T. Kohashi and K. Koike, Jpn. J. Appl. Phys. **40**, L1264 (2001).
36. R. Allenspach, IBM J. Res. Develop. **44**, 553 (2000).
37. See Chapter 4 in [48].
38. E. Kisker, W. Gudat, and K. Schröder, Solid State Commun. **44**, 591 (1982).
39. J. Unguris, D.T. Pierce, A. Galejs, and R.J. Cellota, Phys. Rev. Lett. **49**, 72 (1982).
40. H. Hopster, R. Raue, E. Kisker, G. Güntherodt, and M. Campagna, Phys. Rev. Lett. **50**, 70 (1983).
41. M.S. Hammond, G. Fahsold, and J. Kirschner, Phys. Rev. B **45**, 6131 (1992).
42. J. Kirschner in "Surface and interface characterization by electron optical methods", A. Howie & U. Valdré (eds), Plenum Publishing Corporation, 267.
43. H.C. Siegmann, D.T. Pierce, and R.J. Celotta, Phys. Rev. Lett. **46**, 452 (1981).
44. D. Tillmann, R. Thiel, and E. Kisker, Z. Phys. B **77**, 1 (1989).
45. R. Bertacco, M. Merano, and F. Ciccacci, Appl. Phys. Lett. **72**, 2050 (1998).
46. R. Bertacco, D. Onofrio, and F. Ciccacci, Rev. Sci. Instrum. **70**, 3572 (1999).
47. H.P. Oepen, unpublished.
48. L. Reimer: "Scanning Electron Microscopy: Physics of Image Formation and Microanalysis", Springer Series in Optical Sciences Vol. 45, Berlin, 1985.

49. J. Unguris, M.R. Scheinfein, D.T. Pierce, and R.J. Cellota, Appl. Phys. Lett. **55**, 2553 (1989).
50. A. Hubert and R. Schäfer: "Magnetic Domains: The Analysis of Magnetic Microstructures", Springer, Berlin, 1998.
51. U. Gradmann in "Handbook of Magnetic Materials" Vol. 7, ed. K.H.J. Buschow, North Holland, Amsterdam, 1993.
52. J.A.C. Bland and B. Heinrich (eds.): "Ultrathin Magnetic Structures" Vol. 1 & 2, Springer, Berlin, 1994.
53. M. Farle, Rep. Prog. Phys. **61**, 755 (1998).
54. C. Chappert, D. Renard, P. Beauvillain, J.P. Renard, and J. Seiden, J. Magn. Magn. Mater. **54–57**, 795 (1986).
55. F.J.A. den Broeder, D. Kuiper, A.P. van de Mosselaer, and W. Hoving, Phys. Rev. Lett. **60**, 2769 (1988).
56. C.H. Lee, H. He, F. Lamelas, W. Vavra, C. Uher, and R. Clarke, Phys. Rev. Lett. **62**, 653 (1989).
57. J. Pommier, P. Meyer, G. Pémissard, J. Ferré, P. Bruno, and D. Renard, Phys. Rev. Lett. **65**, 2054 (1990).
58. B. Voigtländer, G. Meyer, and N.M. Amer, Phys. Rev. B **44**, 10354 (1991).
59. M. Speckmann, H.P. Oepen, and H. Ibach, Phys. Rev. Lett. **75**, 2035 (1995).
60. Z. Málek and V. Kamberský, Czech. J. Phys. **21**, 416 (1958).
61. B. Kaplan and G.A. Gehring, J. Magn. Magn. Mater. **128**, 111 (1993).
62. Y.T. Millev and J. Phys. Cond. Matt. **8**, 3671 (1996).
63. H.P. Oepen, M. Speckmann, Y.T. Millev, and J. Kirschner, Phys. Rev. B **55**, 2752 (1997).
64. M. Dreyer, M. Kleiber, A. Wadas, and R. Wiesendanger, Phys. Rev. B **59**, 4273 (1999).
65. P. Beauvillain, A. Bounouh, C. Chappert, R. Mégy, S. Ould-Mahfoud, J.P. Renard, P. Veillet, D. Weller, and J. Corno, J. Appl. Phys. **76**, 6078 (1994).
66. J. Kohlhepp and U. Gradmann, J. Magn. Magn. Mater. **139**, 347 (1995).
67. B.N. Engel, M.H. Wiedmann, R.A. Van Leeuwen, and C.M. Falco, Phys. Rev. B **48**, 9894 (1993).
68. H.B.G. Casimir, J. Smit, U. Enz, J.F. Fast, H.P.J. Wijn, E.W. Gorter, A.J.W. Duyvesteyn, J.D. Fast, and J.J. de Jong, J. Phys. Radium **20**, 360 (1959).
69. Y.T. Millev and J. Kirschner, Phys. Rev. B **54**, 4137 (1996).
70. D.P. Pappas, K.-P. Kämper, and H. Hopster, Phys. Rev. Lett. **64**, 3179 (1990).
71. D.P. Pappas, C.R. Brundle, and H. Hopster, Phys. Rev. B **45**, 8169 (1992).
72. R. Allenspach and A. Bischof, Phys. Rev. Lett. **69**, 3385 (1992).
73. T. Duden and E. Bauer, Mater. Res. Soc. Symp. Proc. **475**, 273 (1997).
74. E.Y. Vedmedenko, H.P. Oepen, and J. Kirschner, Phys. Rev. B submitted.
75. C. Liu, E.R. Moog, and S.D. Bader, Phys. Rev. Lett. **60**, 2422 (1988).
76. J. Thomassen, F. May, B. Feldmann, M. Wuttig, and H. Ibach, Phys. Rev. Lett. **69**, 3831 (1992).
77. C. Kittel, Phys. Rev. **70**, 965 (1946).
78. R. Carey & E.D. Isaac: "Magnetic Domains and Techniques for Their Observation", The English Universities Press Limited, London, 1966.
79. H.P. Oepen, J. Magn. Magn. Mater. **93**, 116 (1991).
80. E. Feldtkeller in Proceedings of the International Symposium held in Clausthal-Göttingen, eds.: R. Niedermayer and H. Mayer, Van de Hoeck & Ruprecht, Göttingen, 1966.
81. P. Krams, F. Lauks, R.L. Stamps, B. Hillebrands, and G. Güntherodt, Phys. Rev. Lett. **69**, 3674 (1992).

82. A. Berger, U. Linke, and H.P. Oepen, Phys. Rev. Lett. **68**, 839 (1992).
83. L. Néel, Compt. Rend. Acad. Sci. Paris, **241**, 533 (1955).
84. E. Feldtkeller, Z. Angew. Phys. **15**, 206 (1963).
85. R. Kirchner and W. Döring, J. Appl. Phys. **39**, 855 (1968).
86. H. Riedel and A. Seeger, Phys. Stat. Sol. (b) **46**, 377 (1971).
87. A. Berger and H.P. Oepen, Phys. Rev. B **45**, 12596 (1992).
88. E.E. Huber Jr., D.O. Smith, and J.B. Goodenough, J. Appl. Phys. **29**, 294 (1958).
89. R.M. Moon, J. Appl. Phys. **30**, 82S (1959).
90. S. Methfessel, S. Middelhook, and H. Thomas, J. Appl. Phys. **31**, 302S (1960).
91. S. Middelhook, J. Appl. Phys. **34**, 1054 (1963).
92. G. Steierl, W. Lutzke, H.P. Oepen, S. Tegen, C.M. Schneider, and J. Kirschner, Magnetoelektronik, Beiträge zum BMBF-Statusseminar Magnetoelektronik, Dresden 2000, VDI-Technologiezentrum, Düsseldorf, 341 (2000).
93. P. Grünberg, R. Schreiber, Y. Pang, M.B. Brodsky, and H. Sowers, Phys. Rev. Lett. **57**, 2442 (1986).
94. M.N. Baibich, J.M. Broto, A. Fert, F. Nguyen Van Dau, F. Petroff, P. Etienne, G. Creuzet, A. Friederich, and J. Chazelas, Phys. Rev. Lett **61**, 2472 (1988).
95. S.S.P. Parkin, N. More, and K.P. Roche, Phys. Rev. Lett. **64**, 2304 (1990).
96. J. Unguris, R.J. Celotta, and D.T. Pierce, Phys. Rev. Lett. **67**, 140 (1991).
97. D.T. Pierce, J.A. Stroscio, J. Unguris, and R.J. Celotta, Phys Rev. B **49**, 14564 (1994).
98. D.T. Pierce, J. Unguris, R.J. Celotta, and M.D. Stiles, J. Magn. Magn. Mater. **200**, 290 (1999).
99. J. Unguris, R.J. Celotta, D.T. Pierce, and J.A. Stroscio, J. Appl. Phys. **73**, 5984 (1993).
100. J. Unguris, R.J. Celotta, and D.T. Pierce, J. Magn. Magn. Mater. **127**, 205 (1993).
101. J. Unguris, R.J. Celotta, and D.T. Pierce, J. Appl. Phys. **75**, 6437 (1994).
102. J. Unguris, R.J. Celotta, and D.T. Pierce, Phys. Rev. Lett. **79**, 2734 (1997).
103. D.A. Tulchinsky, J. Unguris, and R.J. Celotta, J. Magn. Magn. Mater. **212**, 91 (2000).
104. D.T. Pierce, A.D. Davis, J.A. Stroscio, D.A. Tulchinsky, J. Unguris, and R.J. Celotta, J. Magn. Magn. Mater. **222**, 13 (2000).
105. W.H. Meiklejohn and C.P. Bean, Phys. Rev. **102**, 1413 (1956).
106. J. Nouges and I.K. Schuller, J. Magn. Magn. Mater. **192**, 203 (1999).
107. T.G. Walker, A. Pang, H. Hopster, and S.F. Alvarado, Phys. Rev. Lett. **69**, 1121 (1992).
108. T.G. Walker and H. Hopster, Phys. Rev. B **48**, 3563 (1993).
109. J. Unguris, R.J. Cellota and D.T. Pierce, Phys. Rev. Lett. **69**, 1125 (1992).
110. P. Fuchs, V.N. Petrov, K. Totland, and M. Landolt, Phys. Rev. B **54**, 9304 (1996).
111. D.T. Pierce, R.J. Celotta, and J. Unguris, J. Appl. Phys. **73**, 6201 (1993).
112. H. Matsuyama, C. Haginoya, and K. Koike, Phys. Rev. Lett. **85**, 646 (2000).
113. J.C. Sloncewski, Phys Rev. Lett. **67**, 3172 (1991).
114. J.C. Slonczewski, J. Magn. Magn. Mater. **150**, 13 (1995).
115. N.C. Koon, Phys. Rev. Lett. **78**, 4865 (1997).
116. H. Hopster, J. Appl. Phys. **87**, 5475 (2000).
117. T. VanZandt, R. Browning, and M. Landolt, J. Appl. Phys. **69**, 1564 (1991).
118. Y. Iwasaki, K. Bessho,, J. Kondis, H. Ohmori, and H. Hopster, Applied Surface Science **113/114**, 155 (1997).
119. M. Haag and R. Allenspach, Geophysical Research Letters **20**, 1943 (1993).
120. K.J. Kirk, J.N. Chapman, and C.D.W. Wilkinson, Appl. Phys. Lett. **71**, 539 (1997).
121. T. Schrefl, J. Fiedler, K.J. Kirk, and J. Chapman, J. Magn. Magn. Mater. **175**, 193 (1997).
122. G. Steirerl, G. Lin, D. Jorgov, and J. Kirschner, Rev. Sci. Instrum. **73**, 4264 (2002).
123. D.E. Eastman, Phys. Rev. B **2**, 1 (1979)